Can grain size sensitive flow lubricate faults during the initial stages of earthquake propagation?

Nicola De Paola [a,*], Robert E. Holdsworth [a], Cecilia Viti [b], Cristiano Collettini [c,d], Rachael Bullock [a]

[a] Rock Mechanics Laboratory, Earth Sciences Department, Durham University, South Road, Durham, DH1 3LE, UK
[b] Dipartimento di Scienze Fisiche, della Terra e dell'Ambiente, Siena University, Via Laterina 8, 53100 Siena, Italy
[c] Dipartimento di Scienze della Terra, Sapienza Università di Roma, Piazzale Aldo Moro, 5, 00185 Rome, Italy
[d] Istituto Nazionale di Geofisica e Vulcanologia, Sezione Roma 1, Via Vigna Murata 605, I-00143 Rome, Italy

ABSTRACT

Recent friction experiments carried out under upper crustal P–T conditions have shown that microstructures typical of high temperature creep develop in the slip zone of experimental faults. These mechanisms are more commonly thought to control aseismic viscous flow and shear zone strength in the lower crust/upper mantle. In this study, displacement-controlled experiments have been performed on carbonate gouges at seismic slip rates (1 m s^{-1}), to investigate whether they may also control the frictional strength of seismic faults at the higher strain rates attained in the brittle crust. At relatively low displacements (<1 cm) and temperatures ($\leq 100\,^\circ$C), brittle fracturing and cataclasis produce shear localisation and grain size reduction in a thin slip zone (150 μm). With increasing displacement (up to 15 cm) and temperatures (T up to $600\,^\circ$C), due to frictional heating, intracrystalline plasticity mechanisms start to accommodate intragranular strain in the slip zone, and play a key role in producing nanoscale subgrains (≤ 100 nm). With further displacement and temperature rise, the onset of weakening coincides with the formation in the slip zone of equiaxial, nanograin aggregates exhibiting polygonal grain boundaries, no shape or crystal preferred orientation and low dislocation densities, possibly due to high temperature ($>900\,^\circ$C) grain boundary sliding (GBS) deformation mechanisms. The observed micro-textures are strikingly similar to those predicted by theoretical studies, and those observed during experiments on metals and fine-grained carbonates, where superplastic behaviour has been inferred. To a first approximation, the measured drop in strength is in agreement with our flow stress calculations, suggesting that strain could be accommodated more efficiently by these mechanisms within the weaker bulk slip zone, rather than by frictional sliding along the main slip surfaces in the slip zone. Frictionally induced, grainsize-sensitive GBS deformation mechanisms can thus account for the self-lubrication and dynamic weakening of carbonate faults during earthquake propagation in nature.

© 2015 Elsevier B.V. All rights reserved.

1. Introduction

Earthquakes are typically hosted in the shallower portion of crustal fault zones (≤ 15 km depth and ambient $T \leq 300\,^\circ$C), where fracturing and cataclasis are traditionally thought to be the dominant processes during frictional sliding (Kohlstedt et al., 1995; Scholz, 1998; Sibson, 1977). At greater depths and temperatures, in the lower crust/upper mantle, viscous flow, potentially associated with superplastic behaviour (Ashby and Verrall, 1973; Boullier and Gueguen, 1975; Hiraga et al., 2010; Rutter et al., 1994; Schmid et al., 1977; Walker et al., 1990), is inferred to facilitate aseismic creep along shear zones, based on experimental data and microstructural observations (Ashby and Verrall, 1977; Kohlstedt et al., 1995; Passchier and Trouw, 2005; Poirier, 1985; Rutter, 1995, 1999). Grain boundary sliding (GBS) diffusion creep, associated with superplastic behaviour, i.e., the ability of materials to achieve unusually high elongations ($>100\%$) before failure, has been observed at high strain rates ($>10^2 \text{ s}^{-1}$) for a range of nano-phase alloys (Chandra, 2002) and ceramics (Lankford, 1996). These mechanisms could potentially occur in ultrafine-grained (nano-scale) geological materials deformed at higher strain rates and temperatures appropriate for seismic slip or slow earthquakes (Green et al., 2015; Rutter and Brodie, 1988; Schubnel et al., 2013; Verberne et al., 2014).

Recent laboratory experiments, performed using rotary shear apparatuses, show that when sliding at seismic velocities (≥ 0.5 m s^{-1}) the frictional strength of faults, μ, is significantly lower ($\mu = 0.1$–0.3) (Di Toro et al., 2011; Goldsby and Tullis, 2011; Hirose and Shimamoto, 2005; Reches and Lockner, 2010) than when sliding at low (<1 mm s^{-1}), sub-seismic speeds ($\mu = 0.6$–0.85) (Byerlee, 1978). Understanding the processes controlling the evolution of fault strength as seismic slip rates are approached is of paramount importance. Strength cannot be measured directly using seismological data, yet it affects the magnitude of the stress drop, the heat flow signature of seismogenic faults, and the relative partitioning of the earthquake energy budget (i.e., the proportion of energy dissipated as seismic waves that can travel to the Earth's surface and cause damaging earthquakes). It has been proposed that slip weakening of experimental and natural seismic faults is caused by thermally-activated processes triggered by localised frictional heating and high temperatures attained in the slip zone (Rice, 2006). Furthermore, recent studies show that cohesive slip zones (SZs), in natural (Siman-Tov et al., 2013) and experimental carbonate seismic faults (De Paola et al., 2011a, 2011b; Fondriest et al., 2013; Green et al., 2015; Ree et al., 2014; Smith et al., 2013; Verberne et al., 2014), are composed of striated and mirrored slip surfaces (SSs). Microstructural analyses show that the SSs and the adjacent SZ material are made of calcite nanograin ($D < 1$ µm) aggregates with a polygonal texture, a microstructure consistent with deformation by creep deformation mechanisms. The use of mirror SSs and nano-granular SZ textures as indicators of seismic slip on faults in carbonates (e.g. Ree et al., 2014; Smith et al., 2013) has been questioned by Verberne et al. (2013, 2014) who have shown that similar features can develop during low velocity (1 µm s^{-1}) friction experiments performed on simulated calcite gouge at upper crustal P–T conditions. However, the grain-scale processes suggested to account for the observed weakening of rocks deformed in the laboratory at seismic velocities are still debated (De Paola et al., 2011a, 2011b; De Paola, 2013; Han et al., 2010; Tisato et al., 2012), as is their occurrence along natural faults during earthquake propagation. Verberne et al. (2014) performed microstructural analyses on experimentally deformed samples at sub-seismic slip rates (1 µm s^{-1}) and low temperatures ($<140\,^\circ$C). They show that nanofibre formation during nanogranular flow with diffusive mass transfer can promote velocity-weakening behaviour and earthquake nucleation in carbonate rocks. Green et al. (2015) integrated microstructural observations and experimental work to show that mineral phase transformation in carbonate rocks, occurring at the high temperatures produced by frictional heating, can generate nanometric materials which are weak at seismic slip rates (≈ 1 m s^{-1}) and flow by grain-boundary sliding mechanisms.

Here we study the evolution of deformation mechanisms, and their control on the frictional strength of slip zones developed in simulated, carbonate gouges during accelerating sliding to seismic slip rates ($v = 1$ m s^{-1}). To do so we combine results from new laboratory friction experiments with microstructural observations on samples sheared up to the attainment of dynamic weakening, but *prior* to the onset of phase transformation. Flow stress calculations are performed to investigate whether grainsize-sensitive creep deformation mechanisms, potentially associated with superplastic behaviour, can effectively weaken faults and facilitate earthquake propagation in the shallow crust. To illustrate the relevance of our findings to natural faults, we also carried out microstructural observations on the principal slip zone material extracted from natural, seismically active faults in carbonates.

2. Experimental settings

Friction experiments were performed in the Rock Mechanics Laboratory, at Durham University (UK), using a low to high velocity rotary shear apparatus (details in Supplementary Information 1 – Fig. SI1) built by the Marui and Co., Ltd Company (Osaka, Japan). We performed a set of eight displacement-controlled experiments at room temperature and humidity conditions on fine-grained ($63 < D < 93$ µm), carbonate gouges at target slip rates $v = 1$ m s^{-1} and normal stresses $\sigma_n = 12$–18 MPa (Supplementary Information Table 1). During displacement-controlled experiments, arrested at pre-determined displacements, the electric servomotor of the apparatus was controlled in the digital mode, using a signal generator DF1906 (NF corporation) (Supplementary Information 1).

A synthetic fault zone was created by sandwiching 2 g of simulated fault gouge between two stainless steel cylinders (25 mm in diameter), whose ends were machined with radial grooves 500 µm high to grip the sample surface (Supplementary Information 1 – Fig. SI2). The experiments were run under drained conditions, and to limit gouge loss during the experiments, the sample assembly was confined using a Teflon ring. Teflon rings were cut and tightened onto the stainless steel cylinder using a hose clamp. The inner edges of the rings were machined to reduce their sharpness, and thus avoid ring damage and sample contamination by Teflon during the insertion of the stainless steel cylinders (Supplementary Information 1 – Fig. SI2).

Samples were recovered after each experiment to study the slip zone microstructures. Thin sections for optical microscope observations were taken from slices of the slip zone cut at 2/3 of the radius, to make observations consistent with calculated values of the velocity, v, and the displacement d (Supplementary Information 2).

3. Mechanical data

To identify the mechanisms controlling the evolution of friction, we performed a set of displacement-controlled experiments, with a target speed $v = 1$ m s^{-1}, normal stresses $\sigma_n = 12$–18 MPa, and arrested at displacements d from 0.007 to 1.46 m (Supplementary Information Table 1). Experiments arrested at different displacements show similar acceleration paths (Fig. 1a–b), showing that the conditions during our experiments are reproducible (Fig. 1c–d). It also means that microstructures developed at different stages/displacements can be used to study the evolution of deformation mechanisms in the slip zone, and how these may affect frictional strength evolution.

During experiments run up to 1.44–1.46 m total slip, the imposed target speed of 1 m s^{-1} was attained after 0.12 m of slip (Fig. 1a–b). The measured strength consistently showed a four stage evolution (e.g. Exp. Du304–307 in Fig. 1c–d, Supplementary Information Table 1): Stage I) attainment of initial friction values, $\mu_i = 0.67$, upon instantaneous acceleration toward target speed; Stage II) increase in friction up to peak values $\mu_p = 0.80$–0.88, attained just before acceleration to target speed was complete; Stage III) sudden decrease in friction to low steady-state values, $\mu_{ss} = 0.17$–0.21, attained during sliding at constant velocity $v = 1$ m s^{-1}; and Stage IV) sudden increase of friction to $\mu_f = 0.44$–0.45, observed upon deceleration of the motor.

The temperature rise produced during the laboratory experiments has been estimated, to a first approximation, using (Rice, 2006)

$$\Delta T = \frac{\mu \sigma_n \sqrt{vd}}{\rho c_p \sqrt{\pi \kappa}} \tag{1}$$

where μ represents the friction coefficient, σ_n is the normal stress, d is the displacement, ρ is the rock density, c_p is the specific heat
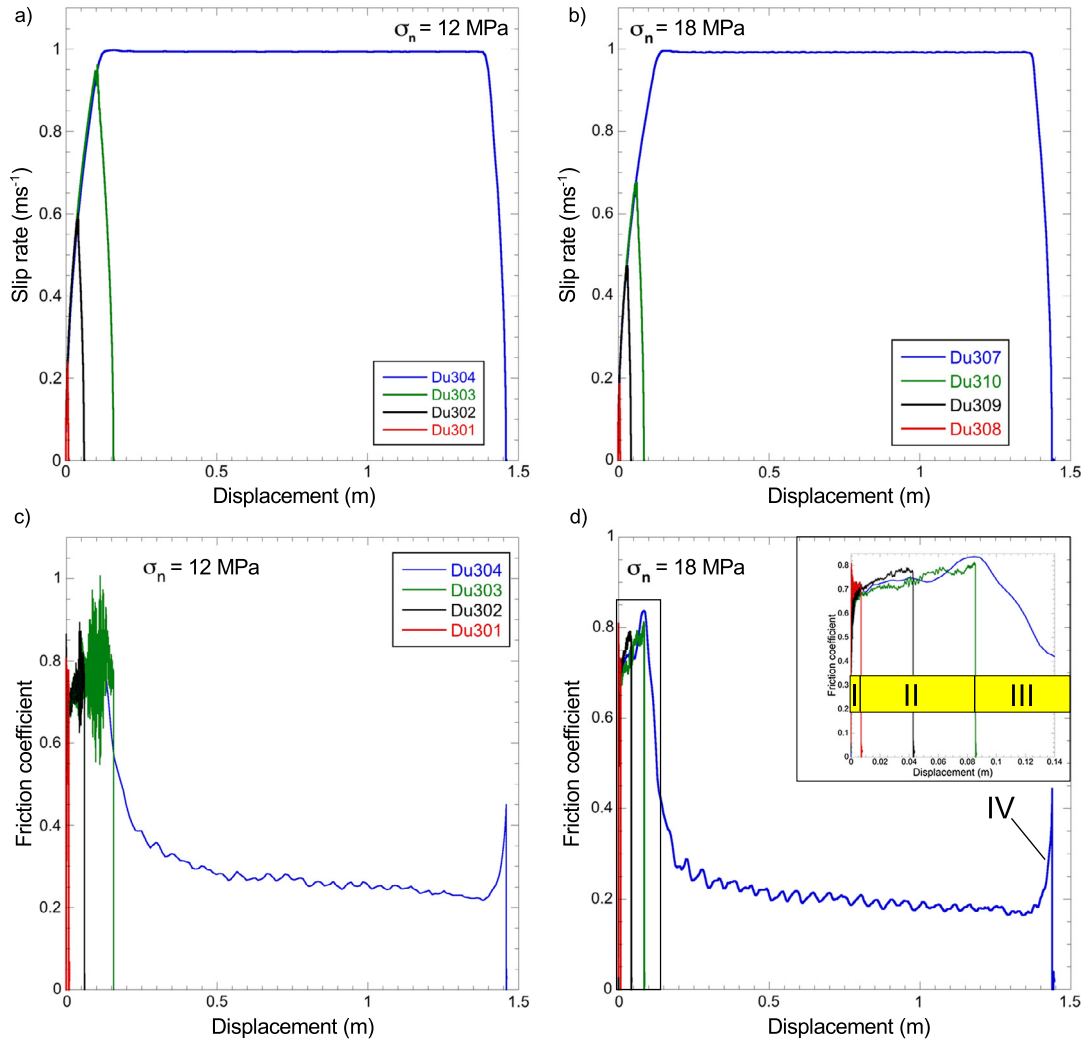
Fig. 1. Experimental data. a–b) Slip rate vs. displacement data for a set of displacement-controlled experiments performed at $\sigma_n = 12$, 18 MPa, and arrested before, during and after the attainment of target speed, $v = 1$ m s^{-1}. c–d) Friction coefficient vs. displacement data showing the evolution of friction during acceleration (Stages I–II), steady-state sliding (Stage III) and instantaneous deceleration to arrest (Stage IV) of the sample. The inset shows a blow-up of the data in the main graph.

capacity and κ is the thermal diffusivity. Microstructural evidence for slip localisation within slip zones with thickness $h < 150$ μm satisfies the condition $h \leq 4\sqrt{\kappa d/v}$, which allows to treat the slip zone as a plane of zero thickness and account for heat diffusion using Eq. (1). For experiments in which steady-state conditions were attained (e.g., Du304 and Du307 in Fig. 1c–d), temperatures were calculated up to the displacements, d_{tr}, attained at the end of the steep drop in friction observed during the transient stage of friction evolution to low, steady-state values, e.g., at $d_{tr} = 0.23$–0.08 m (Supplementary Information Table 1). The contribution to temperature increase by sliding from peak friction values to those attained at d_{tr} was calculated by using the mean value for μ in Eq. (1). The following physical properties of calcite, the main mineralogical component in the deformed rocks, were used for temperature calculations: $\rho = 2700$ kg/m^3, $\kappa = 1.48 * 10^{-6}$ m^2 s^{-1} and $c_p = 700$ J kg^{-1} K^{-1} (Di Toro et al., 2011 and references therein). The mechanical parameters d, μ, σ_n and v used for the temperature calculations are those reported in Supplementary Information Table 1, and the temperatures calculated by Eq. (1) are plotted vs. the measured friction coefficients in Fig. 2. It is observed that friction values are in accord with the range of values predicted by Byerlee's rule for temperatures $\leq 554\,^\circ$C ($\mu_f = 0.68$–0.80), but significantly lower ($\mu_{ss} = 0.17$–0.21) when $T \geq 979\,^\circ$C (Fig. 2).
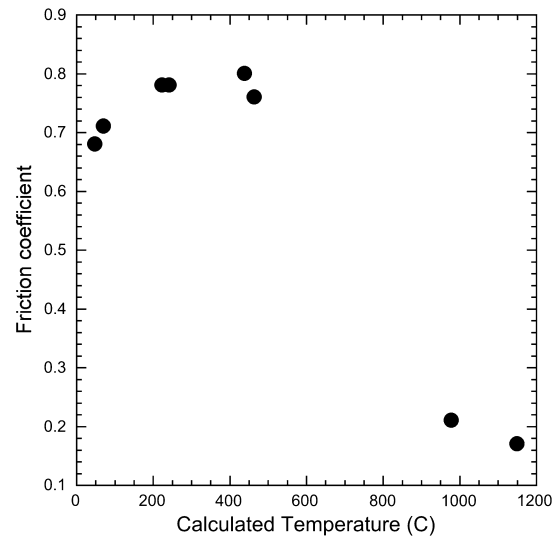

Fig. 2. Temperature vs. friction coefficient data. Temperatures calculated for localised, thin (<150 μm) slip zones plotted vs. the friction coefficient measured during laboratory experiments performed at seismic, target slip rates (1 m s^{-1}) on carbonate gouges (Table 1).
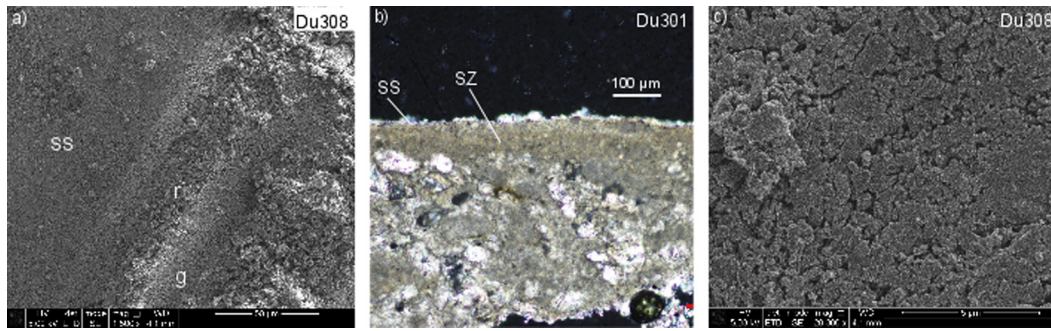
Fig. 3. Microstructural observations of experimental slip zones (Stage I). a) Scanning electron microscope (SEM) image showing in plan view the development of a rough SS, due to the presence of grooves (g) and ridges (r), oriented parallel to the slip direction. b) Optical microscope image showing in cross-section the formation of a continuous, immature slip zone (SZ) with variable thickness (20–200 μm), bounded on the upper part by a rough SS. c) SEM image in plan view showing a magnified, smooth portion of the SS made of fine-grained clasts ($1 < D < 5$ μm), which are sharply truncated against the SS.

4. Microstructural observations and interpretations

4.1. Experimental faults

Samples deformed during Stage I ($d = 0.007$–009 m, Fig. 1c–d) show the formation of an irregular slip zone (SZ) and rough slip surface (SS), due to the presence of grooves (up to 25 μm wide) and ridges, oriented parallel to the slip direction (Fig. 3a). A sharply defined, irregular slip surface (SS) bounds the upper part of the SZ, showing variable thickness (20–200 μm), whilst the lower bound between the SZ and less deformed material is sharp, but rather irregular and wavy (Fig. 3b). The SS is heterogeneous, displaying smooth compact areas interspersed with more granular porous areas (Fig. 3a). The granular portions of the SS appear to be coarser in grain size ($10 < D < 25$ μm) compared to the smooth regions. The smooth portions of the SS are made of fine-grained clasts ($1 < D < 5$ μm), which are sharply truncated against the SS (Fig. 3c). The shape of the clasts on the SS and in the SZ below the SS, is typically angular to sub-angular (Fig. 3c). In places, the smaller clasts display a sub-rounded shape. In the smooth and compact patches, the SS and SZ are still porous, but the porosity, like the grain size, seems finer. Overall, the SZ contains coarse- and fine-grained ($1 < D < 5$ μm), angular clasts, likely formed by brittle fracturing and cataclasis during frictional sliding at low temperatures $< 100\,^{\circ}$C (Fig. 2).

During Stage II, samples show the development of a cohesive SZ, < 150 μm thick (Fig. 4a), containing multiple SSs sandwiching thin layers (tl, ≈ 5 μm) of sub-rounded nanograins (Fig. 4b–c). TEM analyses show that tl contain slightly larger clasts of calcite ($D \leq 1$ μm) dispersed within a porous assemblage of calcite nanograins, ≤ 100 nm in size, with sub-rounded crystal shapes (Fig. 4d). The calcite clasts host dislocations, locally arranged to form dislocation walls separating subgrains ($D \leq 100$ nm) with small angular misorientations; this is typical of low temperature ($\leq 600\,^{\circ}$C) intragranular dislocation creep deformation (Rutter, 1995) (Fig. 4d). Bright-field TEM images show that, together with dislocation walls and subgrain boundaries, calcite clasts (CC) exhibit "damaged" rims, hosting rounded bubbles and lobate, low-contrast features (Fig. 4e). These nanostructures suggest concomitant decarbonation and amorphization processes, preferentially located within the strained calcite rims and at subgrain boundaries. This is where crystal structure defects are concentrated and where, it is suggested, calcite becomes more reactive. We propose that the occurrence of an amorphous phase along subgrain boundaries will facilitate clast disaggregation and the subsequent formation of nano-sized, calcite grain aggregates (Fig. 4d–e). The d-spacing measurements, obtained from the ring-shaped Selected Area Electron Diffraction (SAED) pattern of ultrafine-grained material, confirm that ultrafine grains are composed of calcite

(Fig. 4f). In particular, rings I and II correspond to 3.82 and 3.00 Å spacing (Fig. 4f), in strong agreement with the 3.85 and 3.03 Å of reference calcite (012 and 104 reflections, respectively).

When deforming through Stage III, up to $d = 1.44$–1.46 m (Fig. 1c–d), samples show the localisation of slip in a cohesive SZ, < 150 μm thick, and the formation of shiny, mirror-like SSs (Fig. 5a). The bulk slip zone configuration is similar to those seen during Stage II (Fig. 4a–b), but the grain scale textures are very different. Low porosity SSs ($D \approx 600$–700 nm) separate thin layers of nanograin ($D \approx 100$–600 nm) aggregates with markedly polygonal textures and straight grain boundaries (Fig. 5b–c). SEM images show that the SSs and the thin layers (tl) are composed of relatively compact, polygonal nanostructures of calcite grains, with 120° triple junction contacts between equiaxial grains (Fig. 5b–c). Patches of polygonal nanograins with coarser (600–700 nm, Fig. 5b) and finer (≤ 100 nm, Fig. 5c) grainsize are observed in the tl, in contrast to the polygonal nanograins on the SS which display a more uniform, but larger grainsize distribution (600–700 nm) (Fig. 5b–c). TEM analyses show that the finer and coarser calcite grains in the tl have low dislocation densities, as shown by their homogeneous TEM contrast, regardless of their crystal orientation (Fig. 5d). Relatively large cavities (e.g., C in Fig. 5e) occur along grain boundaries or at triple junctions, whereas smaller rounded bubbles are trapped within calcite grains (Fig. 5e). Calcite clasts from the tl in the SZ exhibit irregular, lobate crystal boundaries, surrounded by thin (< 10 nm) rims of amorphous material of limited extent (Fig. 5f). Calcite grains do not show crystal preferred orientation, as they are characterised by ring-shaped SAED patterns (Fig. 5g). Measured d-spacing confirms that the polygonal grains are calcite (Fig. 5g).

4.2. Phase transformation and annealing processes

We found little evidence for phase transformations that might cause weakening in our experiments. Microstructural and mineralogical observations show that the development of degassing bubbles (Figs. 4e, 5e) and amorphization rims (Figs. 4e, 5f), indicative of decarbonation reactions, are limited to the boundaries of calcite grains in the SZ of samples deformed through Stage II and Stage III. In both cases, SAED pattern analyses revealed that the clasts in the SZ are composed of calcite (Figs. 4f, 5g), confirming that decarbonation reactions in the SZ of samples deformed up to Stage III were not quantitatively significant. We interpret this as being due to the kinetics of the decarbonation reaction requiring exposure to decomposition temperatures for periods much longer than the few fractions of a second that occurred during our experiments (De Paola et al., 2011a). This interpretation is supported by further microstructural evidence showing that widespread and
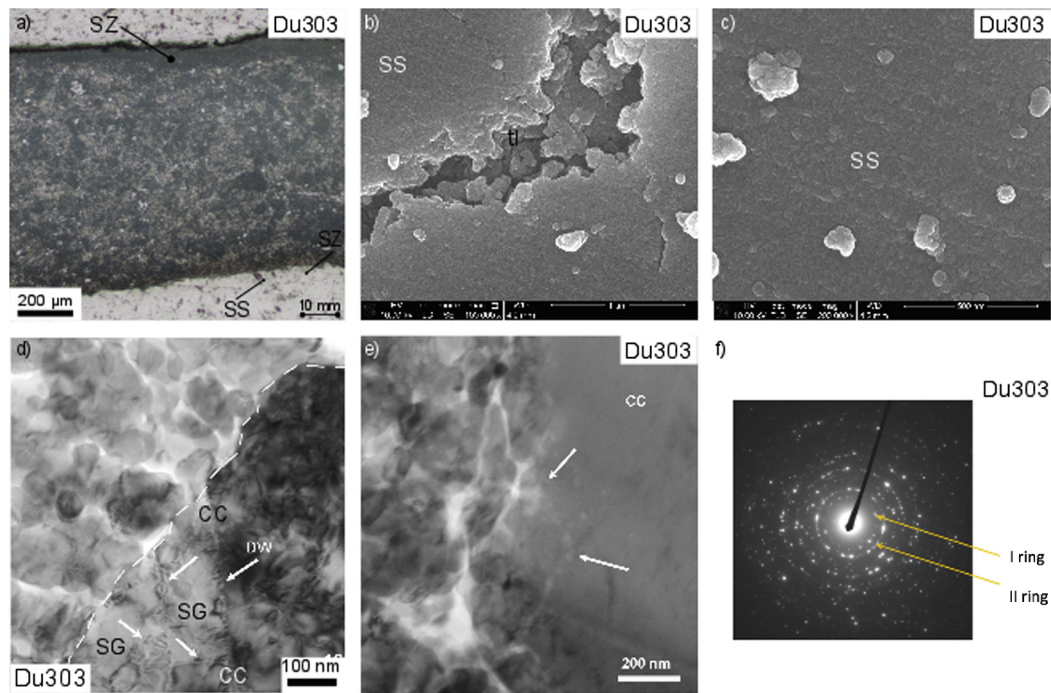
Fig. 4. Microstructural observations of experimental slip zones (Stage II). a–c) Optical microscope (a, cross section view) and SEM (b–c, plan view) images show the development a cohesive slip zone (SZ), and striated slip surface (SS) sandwiching thin layers made of nanograin aggregates ($D \leq 100$ nm) with sub-rounded shape. d) TEM image showing calcite nanograins (≤ 100 nm) in contact with a calcite clast (CC) hosting dislocations and dislocation walls (DW) separating subgrains (SG) ($D \leq 100$ nm). e) Calcite clasts (CC) exhibit "damaged" rims, hosting rounded bubbles and lobate, low-contrast features (arrows) (bright-field TEM images). f) Measured d-spacings from ring-shaped SAED pattern confirm that ultrafine grains are formed by calcite.
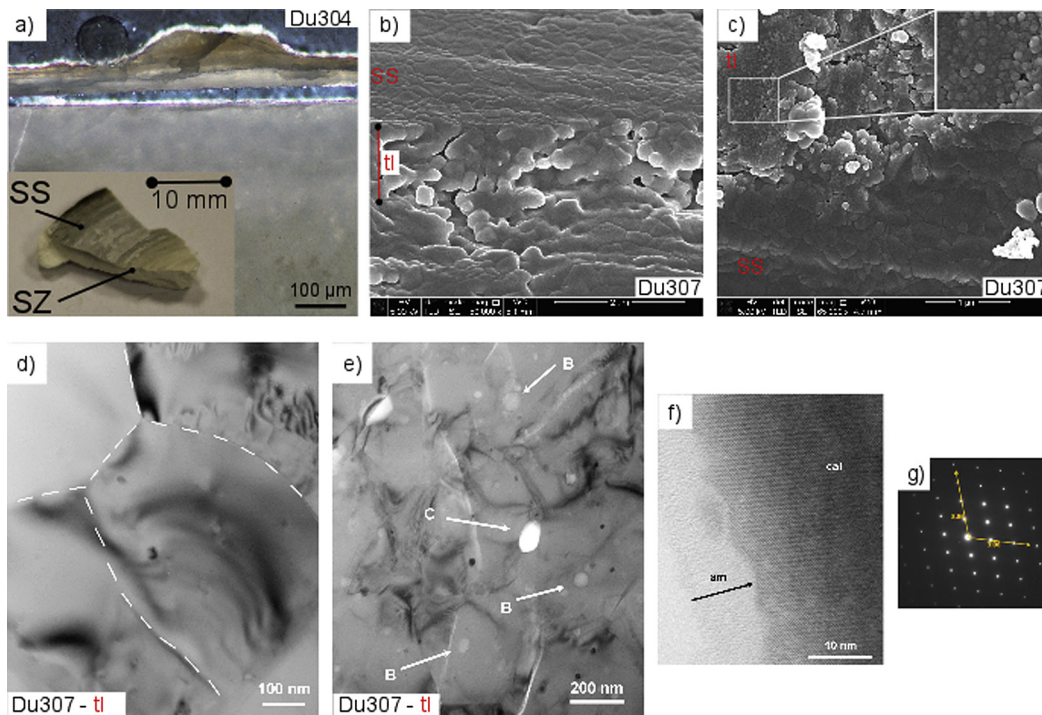

Fig. 5. Microstructural observations of experimental slip zones (Stage III). a–c) Optical microscope (a, cross section and inset oblique plan views) and SEM (b–c, plan view) images show the development of a cohesive slip zone (SZ) composed of stacked striated slip surfaces (SS), sandwiching thin layers (tl) of nanoscale grains. d) TEM images show that tl are associated with compact polygonal nanostructures of calcite grains, displaying low free dislocation densities. e) TEM image of relatively large cavities (C) formed along grain boundaries or at triple junctions, whereas smaller rounded bubbles are trapped within calcite grains (B). f) Calcite clast relic from the thin porous layers in the slip zone (see main text), exhibiting irregular, lobate crystal boundaries, surrounded by a 10 nm thick amorphous rim (am). g) Measured d-spacings from single-crystal SAED pattern of polygonal grains from the thin layers confirm that polygonal grains are formed by calcite (arrows show the corresponding reciprocal axes).

pervasive, intragranular thermal decomposition processes do affect polygonal calcite grains, when high temperatures are maintained for longer time periods (>2 s) during high displacement experiments ($d > 5$ m) (Supplementary Information 2). Thus we propose that the observed weakening is not caused by thermally activated phase transitions when fault displacements are <1.5 m.

Microstructural observations on samples deformed up to Stage III show the presence of localised patches of small (≤ 100 nm) polygonal nanograins in the tl of the SZ. The grainsizes are similar to those observed in the tl of samples deformed up to Stage II (Figs. 4b–d, 5b–c). However, slightly larger polygonal nanograins (600–700 nm) have also been observed on both the SS and in the tl of samples deformed up to Stage III (Fig. 5b–c), suggesting that grain growth processes occurred in the nanograins of the experimental SZ. Grain growth kinetics and the grainsize that can be attained by normal grain growth are described by the well know equation (e.g., Covey-Crump, 1997)

$$d^{\frac{1}{n}} - d_0^{\frac{1}{n}} = k_0 t e^{-\frac{H}{RT}} \tag{2}$$

where d is the grainsize, d_0 is the initial grainsize, t is the duration of the growth period, n is a dimensionless constant which depends on the process controlling the growth rate, k_0 is the pre-exponential factor, H is the apparent activation enthalpy of the process controlling the grain growth, R is the gas constant and T is the temperature. During sample deformation up to Stage II ($T = 500\,°C$) and Stage III ($T = 800$–$1000\,°C$) (Supplementary Information Table 1), the maximum temperatures inferred in the slip zone are only attained for a fraction of a second, and it takes <10 s for our sample to cool down to $T < 100\,°C$. Hence, we assume that $t = 1$ s is a conservative estimation of the time-scale upon which grain growth, due to static recrystallisation, may occur in the slip zone. The parameters $n = 0.5$, $k_0 = 3.5502 * 10^{-10}$ $\mu m^{1/n}\,s^{-1}$ (obtained from $k_{979\,K} = 5.5626 * 10^{-3}$ $\mu m^{1/n}\,s^{-1}$), $H = 240 * 10^3$ $J\,mol^{-1}$, $R = 8.3145$ $J\,K^{-1}\,mol^{-1}$, obtained by Covey-Crump (1997) for the pore-fluid absent conditions, were used to solve Eq. (2), and to calculate the maximum theoretical increase in grain size, d, from an initial grain size $d_0 = 0.1$ μm, when growth time $t = 0.1$, 1, 10 s and temperature $T = 500$, 800, 900, 1000 °C (Fig. 6). The results show that, for conditions similar to those attained in samples deformed up to Stage II (e.g. $T = 500\,°C$ and initial grain size $d_0 = 0.1$ μm), no grain growth should occur in our samples (Fig. 6). Under these conditions, the activation of grain boundary migration processes requires timescales significantly longer than the overall duration and quenching phase of our experiments (Fig. 6). These results agree well with our microstructural observations on SS and tl nanograin aggregates showing $D \leq 100$ nm and a lack of diagnostic large and dislocation-free grains that would be expected to form during annealing.

For conditions similar to those attained in samples deformed up to Stage III (e.g. $T = 800$–$1000\,°C$ and initial grain size $d_0 = 0.1$ μm), grain growth is predicted to occur for the range of time 0.1 s $\leq t \leq 10$ s considered (Fig. 6). At these conditions, grain boundary migration processes could be activated within 0.1 s from the attainment of the high temperatures reached in our experiments when deformed up to Stage III (Fig. 6). Our microstructural observations of polygonal, nanograin aggregates on the SS and in the tl show grain growth from initial values of $d_0 \leq 100$ nm up to $D = 600$–700 nm, which is lower than the maximum grainsize $d = 2.25$ μm predicted by grain growth calculations at $T = 1000\,°C$ and $t = 1$ s (Fig. 6). TEM analyses show that the polygonal calcite grains do have low dislocation density, but there is still a lack of diagnostic large and dislocation-free grains, which would be expected to form during complete annealing. We conclude that static recrystallisation and growth of the nanograin aggregates on the SS and within localised patches in the tl may have occurred after the experiments, during the cooling stage of samples deformed up to Stage III, although the integration of microstructural and theoretical data show that grain growth may only have caused a partial annealing of the original fabric. Elements of this fabric may still be preserved in the tl as patches of fine grainsize polygonal nanograins (see Fig. 5c). The attainment of high T for short durations ($t \leq 1$ s) and the presence of second-phase materials (e.g.,
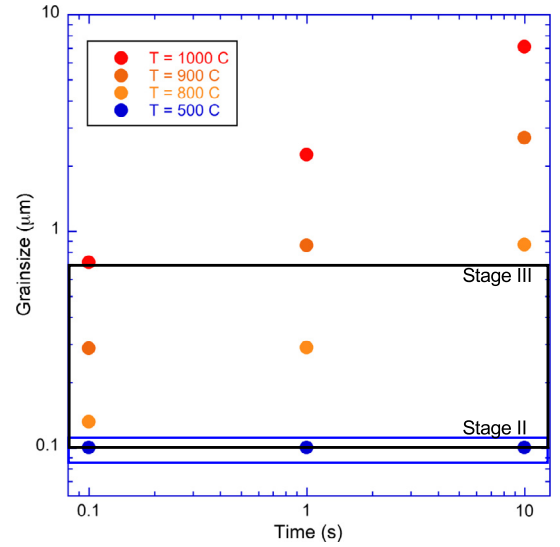

Fig. 6. Modelled grainsize vs. time during static crystallisation. The graph shows the maximum, theoretical increase in grain size, obtained by solving Eq. (2) in the main text for range of temperatures, initial grain sizes and timescales representative of those attained during sample deformation up to Stage II ($T = 500\,°C$) and Stage III ($T = 800$–$1000\,°C$). The blue (Stage II) and black (Stage III) rectangles show the range of grainsizes observed in the experimental slip zones.

amorphous decomposed material, Fig. 5f) and pores (e.g., degassing bubbles, Fig. 5e) pinning the grain boundaries (Olgaard and Evans, 1986), may have limited grain growth during our experiments. This plausibly explains the local preservation of patches of finer polygonal nanograins and the lower grainsizes observed than those theoretically predicted (Fig. 6).

5. Natural faults

In the last decade a series of studies have documented the nucleation and/or propagation of significant earthquakes through thick sequences of carbonates (e.g. Valoroso et al., 2014). Motivated by these observations, several workers have focused on the study of carbonate-bearing faults exhumed from the seismogenic crust in order to improve the characterisation of fault zone structure and deformation processes (e.g. De Paola et al., 2008; Smith et al., 2011; Rowe et al., 2012; Collettini et al., 2013; Siman-Tov et al., 2013; Bullock et al., 2014). Here as a natural example, we use a large-offset (≈ 600 m) fault exposed in the seismic belt of the Apennines, Italy. The fault is 10 km long with a maximum width of about 1.5 km and consists of 5 sub-parallel segments (Collettini et al., 2014). At the outcrop scale the fault structure is characterised by striated and mirrored SSs (Fig. 7a), similar to those observed in other carbonate-hosted, seismically active faults (Smith et al., 2013; Siman-Tov et al., 2013). Sampling and microstructural studies across the SS reveal a natural cohesive SZ (<150 μm thick) characterised by parallel SSs (Fig. 7b, c).

SEM investigations of the SZ show calcite grains with lobate and faint grain boundaries. Grain boundaries are characterised by the concentration of voids and/or vesicles, indicating limited thermal decomposition of calcite (Fig. 7b and Collettini et al., 2014). TEM analyses show that some portions of the SSs and the SZ material are made of micrometre-sized calcite crystals, which commonly show nanoscale polysynthetic twinning. High dislocation densities and subgrain boundary formation indicate that twin lamellae have experienced intense strain. The pervasive occurrence of subgrain boundaries along twinning planes suggests that twinning predates the development of dislocations, dislocation walls and calcite nanograins ($D = 200$–300 nm). Other portions of the SSs and SZ material show calcite nanograin ($D \leq 100$ nm) aggre-
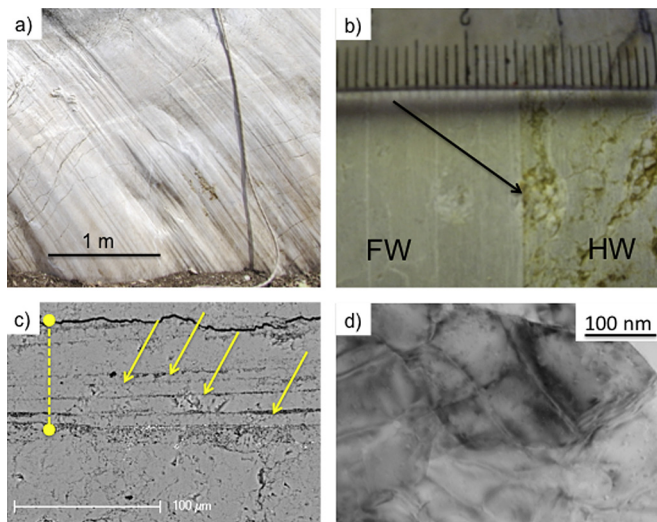
Fig. 7. Mesoscale and microstructural observations from natural slip zones. a) Outcrop photograph of the M. Maggio fault plane, located in the Apennines of Italy (details in Collettini et al., 2014), showing its naturally polished, reflective glossy surface. b) Rock sample cross section including hanging-wall, HW, and footwall, FW, blocks together with the principal slipping zone (indicated by the arrow) where we performed the microstructural studies. c) BSE-SEM image in cross section showing that the principal slipping zone is about 100 mm thick (dashed yellow line) and, here, the slip is accommodated along sub-parallel SSs indicated by yellow arrows. d) Nanostructure composed of polygonal calcite grains in close association with strain-free calcite crystals.

gates with a polygonal texture; the nanograins have straight grain boundaries with 120° triple junction contacts between equiaxial grains, and display no preferred elongation (Fig. 7d). These natural microstructures are strikingly similar to those observed in the experimentally deformed samples during Stage III (Fig. 5c).

6. Discussion

6.1. Micro-scale deformation mechanisms during earthquake propagation

In the experimental samples, a localised slip zone, up to 150 µm thick, develops in the early stages of deformation (Stage I) when the SZ material is poorly consolidated, bounded by slip surfaces, and made of fine-grained, angular clasts ($1 \leq D \leq 5$ µm). Brittle fracturing and cataclasis are the dominant deformation mechanisms observed in samples deformed up to Stage I, at relatively low temperatures ($\leq 100\,^{\circ}$C), and it is these mechanisms that

likely control shear localisation and grain size reduction in the slip zone (Fig. 3) (Bullock et al., 2015; Smith et al., 2015). In our experiments – unlike those of Verberne et al. (2014) – we do not observe the development of shiny, mirror-like slip surfaces and of nanoscale materials in the SZ of samples deformed up to Stage I (up to 7 mm slip). Sliding friction values predicted by Byerlee's rule (Byerlee, 1978) match those measured during experiments arrested in Stage I (Fig. 1).

SEM analyses of samples deformed up to Stage II show that the SZ material becomes cohesive and contains multiple SSs, which sandwich thin (≈ 5 µm) porous layers of sub-rounded nanograins (Fig. 4). TEM analyses show larger clasts of calcite ($D \approx 1$ µm) dispersed within a porous assemblage of calcite nanograins, ≤ 100 nm in size. These larger calcite clasts exhibit a high density of free dislocations and host subgrains ($D \leq 100$ nm) (Fig. 4d–e). As temperatures rise during Stage II, due to frictional heating ($T \approx 550\,^{\circ}$C), intracrystalline plasticity mechanisms, active at $T \leq 600\,^{\circ}$C, start to accommodate intragranular strain and the development of nanoscale subgrains ($D \leq 100$ nm) in the thin layers of the slip zone (Fig. 4d–e).

When deformation progresses through Stage III, samples show a bulk slip-zone configuration similar to Stage II, but the grain-scale microstructures are very different. SEM and TEM analyses of thin layers of nanograin ($D \approx 100$–600 nm) aggregates between the SSs exhibit polygonal grain boundaries, showing 120° triple junctions between equiaxial grains (Fig. 5b–e). The grains display no preferred elongation, no crystal preferred orientation (based on SAED measurements) and low dislocation densities (Fig. 5d–g), possibly due to high temperature ($\geq 900\,^{\circ}$C) GBS deformation mechanisms. The observed micro-textures in experimental (Fig. 8a) and natural slip zones (Fig. 8b) are strikingly similar to those predicted by theoretical studies (Fig. 8c, Ashby and Verrall, 1973), and those observed during experiments on metals (Chandra, 2002) and fine-grained carbonates (Walker et al., 1990; Schmid et al., 1977), at temperatures $\leq 1000\,^{\circ}$C, where superplastic behaviour due to grainsize-sensitive GBS has been inferred. Hence, we propose that the preservation of equiaxial polygonal nano-grains ($D \leq 100$ nm), with low dislocation densities, is diagnostic of GBS mechanisms associated with superplastic behaviour (Verberne et al., 2013, 2014).

Our SEM and TEM observations show that the synthetic carbonate gouges deformed up to Stage III in our experiments preserve microstructural evidence for the operation of GBS accommodated by *both* diffusion and dislocation creep (Fig. 5c–e). The polygonal nanograins developed during Stage III are characterised by a much lower dislocation density compared to those observed during Stage II. This may be due to the establishment of less favourable
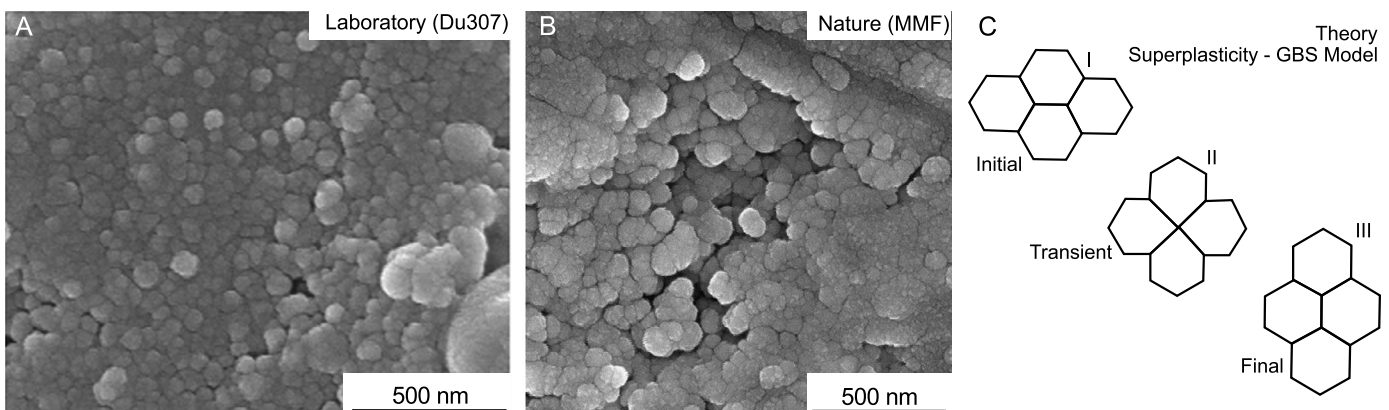

Fig. 8. Microstructures diagnostic of superplastic behaviour: theory vs. experimental/natural slip zone samples. a–b) SEM images of experimental (a) and natural (b) slip zones made of compact calcite nanograin aggregates with a polygonal texture, diagnostic of grainsize sensitive grain boundary sliding (GBS) mechanisms. c) Diagnostic microstructures predicted by superplastic flow accommodated by grainsize sensitive GBS, showing different stages (I–III) of the neighbour switching process (after Ashby and Verrall, 1973).

conditions for the operation of dislocation creep (i.e., high T, small grain size) attained at the transition from Stage II to Stage III in our experiments. Despite microstructural evidence for the simultaneous occurrence and operation of both diffusion- and dislocation-dominated GBS, more microstructural work is needed to quantify their relative contribution to the deformation of nanoscale materials at high strain rates and temperatures. Overall, the distinctive textures observed indicate a switch from low-temperature plasticity and cataclasis (Stages I, II) to GBS mechanisms (Stage III).

Finally, we suggest that the re-strengthening observed during deceleration at the end of the friction experiments (Stage IV, Fig. 1c–d) results from a decrease in the activity of slip zone-localised GBS associated with decreasing temperatures.

6.2. Slip zone strength: can grain size sensitive creep control fault strength during earthquake propagation?

Our experimental results and microstructural observations reveal evidence for the operation of both intracrystalline plasticity and GBS-accommodated flow processes in slip zones deformed at earthquake velocities. The evolution of distinctive micro-textures observed in the slip zone suggests that the transition from low-temperature plasticity and cataclasis ($T \leq 500\,°C$ during Stages I and II, Figs. 2–4) to GBS-accommodated flow ($T \geq 800\,°C$ during Stage III, Figs. 2, 5, 8) coincides with the onset of the weakening measured in the tested materials at seismic conditions (Figs. 1–2). Verberne et al. (2014) were the first to speculate that GBS-accommodated flow could occur at high strain rates and temperatures during rupture propagation in carbonate rocks. Green et al. (2015) produced further experimental evidence for the occurrence of phase transformation and GBS-accommodated flow in carbonate rocks shearing at seismic slip rates and temperatures, and proposed that these mechanisms could be associated with the onset of dynamic weakening in carbonate rocks. In our experiments, phase transformations, such as decarbonation of calcite, that might lead to weakening are of limited extent. Hence, whilst we agree with the previous hypotheses that GBS-accommodated flow can weaken faults at seismic slip rates (Green et al., 2015; Verberne et al., 2014), we suggest that the onset of the observed weakening does not require thermally-activated phase transitions to occur in carbonate rocks.

We now calculate flow stresses to add new evidence to the hypothesis that GBS-accommodated flow can weaken faults at high strain rates and temperatures, prior to the onset of phase transformations, and thus control earthquake propagation in the shallow crust. We use published constitutive flow laws for both dislocation creep and diffusion-dominated GBS in carbonates at temperatures $\geq 500\,°C$ (Ashby and Verrall, 1973; Schmid et al., 1977; Walker et al., 1990), applying a range of strain rates and grain sizes representative of our experimental conditions (Supplementary Information Table 1).

6.2.1. Flow laws and state variables

The predicted flow stress for end-member type deformation mechanisms, dislocation creep and diffusion creep, can be modelled by the constitutive flow law

$$\dot{\gamma} = A^* D^{-b} e^{-\frac{H}{RT}} \tau^n \tag{3}$$

where $\dot{\gamma}$ is the shear strain rate, A^* is a pre-exponential factor, H is the apparent activation energy for creep, R is the gas constant, T is the absolute temperature, τ is the shear stress, n the stress exponent, D is the grain size and b is the grain size exponent. For dislocation creep, b is 0 and $3 < n < 7$, whereas for diffusion creep (which must include GBS) $2 < b < 3$ and $n = 1$. For dislocation-accommodated GBS, b and n lie somewhere between

these two end members, so that $1 < n < 3$ values are predicted for grainsize-sensitive creep regimes (Ashby and Verrall, 1973), when the superposition of the two end-member mechanisms accommodates viscous flow (Ashby and Verrall, 1973; Schmidt et al., 1977). In the latter case ($1 < n < 3$), the overall creep rate should be given, to a sufficient approximation, by their relative contribution (Ashby and Verrall, 1973).

The parameters $b = 0$, $n = 4.70$, $A = 0.046$ (s^{-1} bar^{-n}), $H = 71$ ($kcal\,mol^{-1}$), $R = 1.987 * 10^{-3}$ ($kcal\,K\,mol^{-1}$), and $b = 3$, $n = 1.7$, $A^* = 9.55 * 10^4$ (s^{-1} bar^{-n}), $H = 51$ ($kcal\,mol^{-1}$), $R = 1.987 * 10^{-3}$ ($kcal\,K\,mol^{-1}$), obtained for deformed calcite aggregates from Schmid et al. (1977), were used to solve Eq. (3) and to calculate the flow stress τ predicted for dislocation creep and grainsize-sensitive GBS-accommodated flow, respectively, when $T = 600$, $1000\,°C$ and $\dot{\gamma} = 1$–$3 * 10^3$ s^{-1} (Fig. 9).

The average shear strain, γ, values have been calculated by $\gamma = \tan\phi = r\theta/2h$, where ϕ is the angular shear, r is the outer diameter of the sample, θ is the angular displacement in radians and h is the average slip zone thickness. Shear strain rate, $\dot{\gamma}$, can then be calculated as the ratio $\dot{\gamma} = \Delta\gamma/\Delta t$, where Δt is the duration of each experiment from the onset of a specific deformation mechanism. An average value, $h = 150\,\mu m$, has been assumed during shear strain calculations, based on optical and scanning electron microscope images, which show the development of a slip zone, due to shear localisation, from the very early stages of deformation when d is only a few mm (Fig. 3a). Strain rate values calculated for each deformation mechanism observed during the different stages of the experiments have been used as reference values during the flow stress calculations (Fig. 9, Table 1). The grain size range $D = 10$–600 nm was used during flow stress calculation of grainsize-sensitive GBS-accommodated flow, based on microstructural observations of the slip zone material produced during Stage II and Stage III deformation (Figs. 4–5).

6.2.2. Flow stress values and interpretation of results

Flow stress calculations, performed using Eq. (3), show that dislocation creep mechanisms operate at higher flow stress values ($\tau > 100$ MPa) than grainsize-sensitive GBS in the range of temperatures ($T = 600$–$1000\,°C$) and strain rates ($\dot{\gamma} = 1$–$3 * 10^3$ s^{-1}) considered, when grain size $D < 600$ nm (Fig. 9). For a given temperature, the flow stress increases with strain rate at a steeper gradient during GBS than during dislocation creep (Fig. 9). For a given temperature and a fixed strain rate, the flow stress due to GBS decreases with grain size (Fig. 9). At $T = 600\,°C$ and high strain rates ($\dot{\gamma} \geq 1000$ s^{-1}), the two mechanisms would operate at similar, very high flow stress values ($\tau \approx 3000$ MPa) for a grain size of about 100 nm (Fig. 9a). Under these conditions, the calculated flow stress values are always significantly higher than the values measured during our laboratory experiments (Fig. 9a). At $T = 1000\,°C$ and high strain rates ($\dot{\gamma} \geq 1000$ s^{-1}), grainsize-sensitive GBS flow would operate at much lower flow stress values ($\tau \leq 12$ MPa) than dislocation creep ($\tau \approx 100$ MPa), for grainsize $D \leq 100$ nm (Fig. 9b). Under these conditions, the shear stress values measured during our laboratory experiments are between the calculated flow stress values for grainsize $10 < D < 100$ nm (Fig. 9b).

Our microstructural observations suggest that brittle fracturing and cataclasis are the mechanisms that control shear localisation and grain size reduction in the slip zone at relatively low temperatures ($\leq 100\,°C$). Stress levels predicted by Byerlee's sliding friction values (Byerlee, 1978) match those measured during Stage I (Fig. 10). Very little is known about how grain size reduction to submicron levels actually occurs under the conditions attained during our experiments ($T \geq 500\,°C$), where samples have been deformed up to Stage II (Green et al., 2015; Verberne et al., 2013, 2014). Here, we propose that, as temperatures rise during Stage II, due to frictional heating ($\geq 500\,°C$), dislocation creep
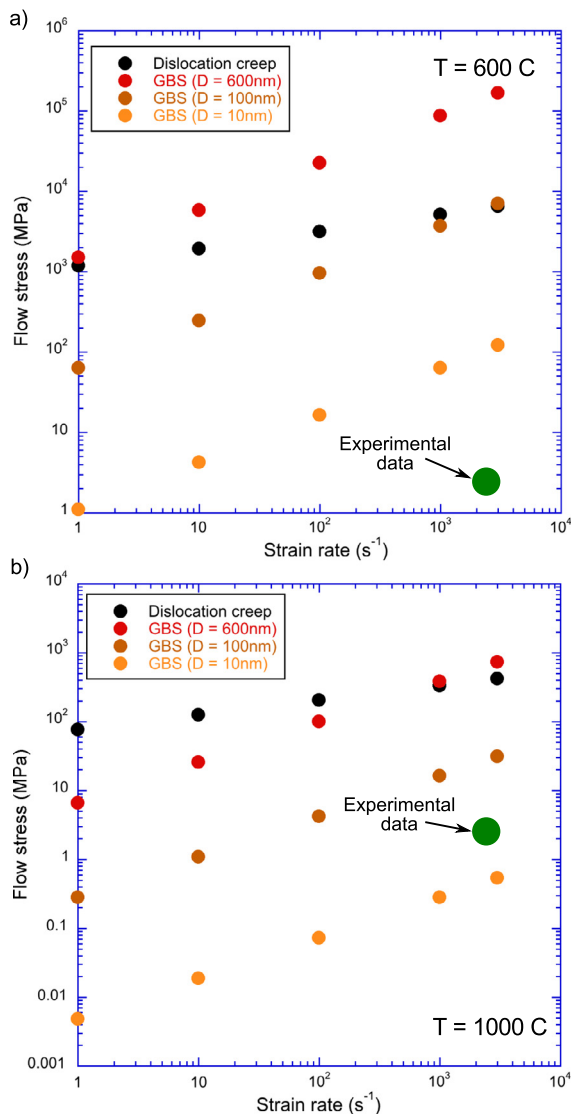
Fig. 9. Measured and predicted flow stresses. a–b) Calculated flow stresses for dislocation creep and grainsize sensitive GBS creep (Eq. (2) in the main text) are plotted vs. strain rates for a range of grain sizes (GBS only) and temperatures, representative of the conditions attained during sample deformation up to Stage II (a) and Stage III (b). The green dots represent the measured shear stress attained in our experiments at steady state during deformation up to Stage III.

Fig. 10. Fault strength evolution with increasing temperatures at high strain rates. Shear stresses predicted by frictional sliding (Byerlee, 1978) match those measured during laboratory experiments at seismic slip rates during Stages I–II (temperature $\leq 600\,^\circ$C). Flow stress values predicted by a regime of grainsize-sensitive GBS creep (Eq. (2) constitutive law in the main text) at temperatures $\geq 600\,^\circ$C, strain rates $= 3 * 10^3$ s^{-1} and grainsize $D < 100$ nm, observed in the slip zone at the onset of weakening, are lower than those predicted by Byerlee's friction, and within the same order of magnitude as the values measured during the experiments during Stage III.

(Fig. 5). Under these temperature and strain rate conditions, the flow stresses predicted for grainsize-sensitive GBS-accommodated flow, for grain size $D < 100$ nm observed in the slip zone at the onset of weakening, are lower than those predicted by Byerlee's friction and, within the same order of magnitude as the values measured during the experiments (Fig. 10).

Our microstructural observations are similar to those of previous studies showing that, under certain conditions, fine-grained geological materials deform by diffusion-accommodated GBS and dislocation-accommodated GBS (Schmid et al., 1977; Walker et al., 1990). This combination of mechanisms appears to be capable of explaining not only the observed relation between strain rate and stress (Schmid et al., 1977; Walker et al., 1990; Hirth and Kohlstedt, 2003; Mecklenburgh et al., 2010; Goldsby and Kohlstedt, 2001), but also most of the microstructural and topological features of materials displaying superplastic behaviour (Ashby and Verrall, 1973; Schmid et al., 1977; Walker et al., 1990; Hirth and Kohlstedt, 2003; Mecklenburgh et al., 2010; Goldsby and Kohlstedt, 2001; Verberne et al., 2014; Green et al., 2015).

We propose therefore that the activation of grainsize-sensitive GBS deformation mechanisms in the nanograin aggregates ($D <$ 100 nm) of the localised slip zone, at high temperatures ($T \approx$ 1000 $^\circ$C) and strain rates $\dot\gamma \geq 1000$ s^{-1}, controls the onset of dynamic weakening of carbonate faults at seismic slip rates (Fig. 10). Note, however, that the cataclasis and intragranular dislocation creep operating during the earlier stages of slip are critical, precursory processes needed to produce the nanoscale grain sizes required to activate grainsize-sensitive creep mechanisms. Finally, the re-strengthening observed during the decelerating phase of deformation can be explained by the falling temperature "switching off" slip zone-localised GBS flow, leading to a return to frictional sliding.

mechanisms start to accommodate intragranular strain and play a key role in producing nanoscale subgrains ($D \leq 100$ nm) in the slip zone (Fig. 4). Note that during Stage II, nanoparticles are present in the slip zone and seismic slip rates have been attained. However, the measured frictional strength of the experimental faults still lies within Byerlee's range of values $\mu = 0.68$–0.80 (Fig. 1, Supplementary Information Table 1). In the absence of microstructural evidence for the operation of pressure solution or diffusion creep (e.g., Verberne et al., 2014), it is suggested that the slip zone bulk strength at this stage is still controlled by cataclastic frictional sliding rather than by dislocation creep or nanopowder lubrication mechanisms. This is in accord with our flow stress calculations, which predict flow stresses for dislocation creep that are up to about 3 orders of magnitude higher than the measured ones at $T = 600\,^\circ$C and $\dot\gamma \geq 1 * 10^2$ s^{-1} (Figs. 9a, 10). When $T \approx 1000\,^\circ$C and $\dot\gamma \approx 3 * 10^3$ s^{-1} are attained during Stage III, micro-textures diagnostic of both dislocation creep and grainsize-sensitive GBS are observed, the latter becoming widespread within the slip zone
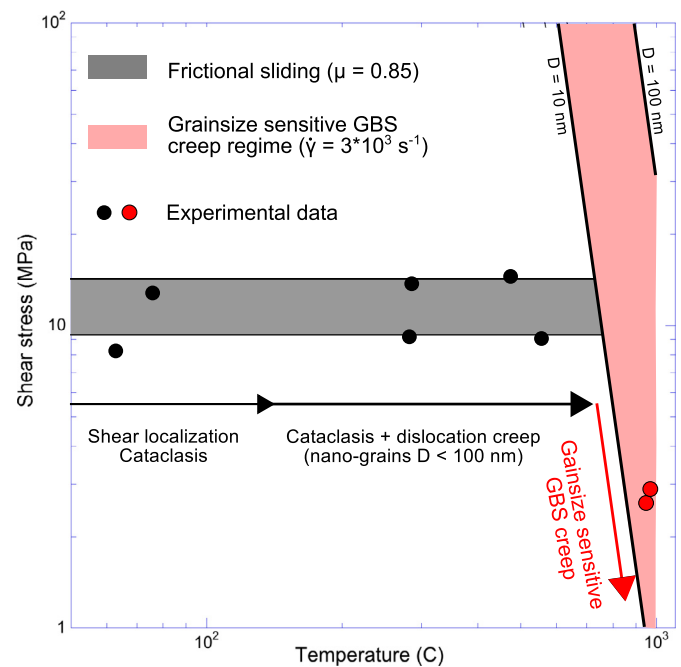
6.2.3. Limitations and approximation of flow stress calculations and interpretations

The calculated flow stress values have been obtained by extrapolating published constitutive flow laws for grainsize-sensitive GBS in carbonates to the conditions attained during our experiments (Fig. 9, Supplementary Information Table 1). The flow stress values obtained for the temperatures, strain rates and grain sizes attained during our experiments, at the onset of weakening, are within about one order of magnitude of those measured during our experiments (Figs. 9–10). The remaining discrepancies are likely due to the approximation of the estimated slip zone parameters (e.g., grain size and SZ thickness), the experimental conditions (γ), and the simplistic extrapolation of existing flow laws to smaller, submicron grain sizes and to strain rates which are a few orders of magnitude higher than those at which they were obtained.

In our study we provide evidence that the onset of weakening during shearing at high velocity coincides with the activation of thermally-induced deformation mechanisms (e.g., grainsize-sensitive GBS) within thin layers of nanograins sandwiched by slip surfaces. To a first approximation, the measured drop in strength is in agreement with our flow stress calculations, suggesting that strain could be accommodated more efficiently by these mechanisms within the weaker thin layers than by frictional sliding along the SS (Fig. 5b–c). A quantitative estimation of the strain partitioning between sliding along the SS and deformation within the thin layers will allow the conceptual model described above to be proven, and provide more constrained strain rate values to be applied in the flow stress calculations. At the present stage, these tasks still present some significant practical challenges in rotary shear apparatus experiments and advanced microstructural studies on the deformed materials.

7. Conclusions

Our observations of experimentally and naturally produced carbonate faults suggest that grainsize-sensitive GBS deformation mechanisms can operate in geological materials deformed at high strain rates along frictionally heated seismogenic slip surfaces at the onset of dynamic weakening after a few centimetres of slip ($d > 10$ cm), before the occurrence of bulk phase transformations. The observed microstructures are similar to those seen at low and high strain rates in carbonates (Verberne et al., 2014; Green et al., 2015), and at high strain rates for a range of nanophase alloys and ceramics in association with superplastic behaviour, where grainsize-sensitive creep regimes develop due to the combined operation of dislocation/diffusion creep. Our findings provide a plausible explanation for both the low flow stresses measured at seismic slip rates in carbonate rocks, and most of the microstructural and topological features of the deformed materials. A regime of frictionally-induced grainsize-sensitive GBS can thus account for the self-lubrication and dynamic weakening of carbonate faults during earthquake propagation in nature.

Acknowledgements

Appendix A. Supplementary material

Supplementary material related to this article can be found online at http://dx.doi.org/10.1016/j.epsl.2015.09.002.

References

Ashby, M.F., Verrall, R.A., 1973. Diffusion-accommodated flow and superplasticity. Acta Metall. 21, 149–163.

Ashby, M.F., Verrall, R.A., 1977. Micromechanics of flow and fracture, and their relevance to the rheology of the upper mantle. Philos. Trans. R. Soc. Lond. 288, 59–95.

Boullier, A.M., Gueguen, Y., 1975. Sp-mylonites – origin of some mylonites by superplastic flow. Contrib. Mineral. Petrol. 50, 93–104.

Bullock, R.J., De Paola, N., Holdsworth, R.E., Trabucho-Alexandre, J., 2014. Lithological controls on the deformation mechanisms operating within carbonate-hosted faults during the seismic cycle. J. Struct. Geol. 58, 22–42.

Bullock, R.J., De Paola, N., Holdsworth, R.E., 2015. An experimental investigation into the role of phyllosilicate content on earthquake propagation during seismic slip in carbonate faults. J. Geophys. Res., Solid Earth 120 (5), 3187–3207.

Byerlee, J., 1978. Friction of rocks. Pure Appl. Geophys. 116, 615–626.

Chandra, N., 2002. Constitutive behavior of superplastic materials. Int. J. Non-Linear Mech. 37, 461–484.

Collettini, C., Viti, C., Tesei, T., Mollo, S., 2013. Thermal decomposition along natural faults during earthquakes. Geology 41, 927–930. http://dx.doi.org/10.1130/G34421.1.

Collettini, C., Carpenter, B.M., Viti, C., Cruciani, F., Mollto, S., Tesei, T., Trippetta, F., Valoroso, L., Chiaraluce, L., 2014. Fault structure and slip localization in carbonate bearing normal faults: an example from the Northern Apennines of Italy. J. Struct. Geol. 67, 154–166. http://dx.doi.org/10.1016/j.jsg.2014.07.017.

Covey-Crump, S.J., 1997. The normal grain growth behaviour of nominally pure calcitic aggregates. Contrib. Mineral. Petrol. 129, 239–254.

De Paola, N., 2013. Nano-powder coating can make fault surfaces smooth and shiny: implications for fault mechanics? Geology 41, 719–720.

De Paola, N., Collettini, C., Faulkner, D.R., Trippetta, F., 2008. Fault zone architecture and deformation processes within evaporitic rocks in the upper crust. Tectonics 27. http://dx.doi.org/10.1029/2007TC002230.

De Paola, N., Chiodini, G., Hirose, T., Cardellini, C., Caliro, S., Shimamoto, T., 2011a. The geochemical signature caused by earthquake propagation in carbonate-hosted faults. Earth Planet. Sci. Lett. 310 (3–4), 225–232.

De Paola, N., Hirose, T., Mitchell, T., Di Toro, G., Viti, C., Shimamoto, T., 2011b. Fault lubrication and earthquake propagation in thermally unstable rocks. Geology 39, 35–38.

Di Toro, G., Han, R., Hirose, T., De Paola, N., Nielsen, S., Mizoguchi, K., Ferri, F., Cocco, M., Shimamoto, T., 2011. Fault lubrication during earthquakes. Nature 471, 494.

Fondriest, M., Smith, S.A.F., Candela, T., Nielsen, S.B., Mair, K., Di Toro, G., 2013. Mirror-like faults and power dissipation during earthquakes. Geology 41, 1175–1178.

Goldsby, D.L., Kohlstedt, D.L., 2001. Superplastic deformation of ice: experimental observations. J. Geophys. Res., Solid Earth 106, 11017–11030.

Goldsby, D.L., Tullis, T.E., 2011. Flash heating leads to low frictional strength of crustal rocks at earthquake slip rates. Science 334, 216–218.

Green, H.W., Shi, F., Bozhilov, K., Xia, G., Reches, Z., 2015. Phase transformation and nanometric flow cause extreme weakening during faulting. Nat. Geosci. http://dx.doi.org/10.1038/NGEO2436.

Han, R., Hirose, T., Shimamoto, T., 2010. Strong velocity weakening and powder lubrication of simulated carbonate faults at seismic slip rates. J. Geophys. Res., Solid Earth 115 (B3). http://dx.doi.org/10.1029/2008JB006136.

Hiraga, T., Miyazaki, T., Tasaka, M., Yoshida, H., 2010. Mantle superplasticity and its self-made demise. Nature 468, 1091–1490.

Hirose, T., Shimamoto, T., 2005. Growth of molten zone as a mechanism of slip weakening of simulated faults in gabbro during frictional melting. J. Geophys. Res., Solid Earth 110 (B5). http://dx.doi.org/10.1029/2004JB003207.

Hirth, G., Kohlstedt, D.L., 2003. In: Eiler, J. (Ed.), Inside the Subduction Factory. American Geophysical Union, Washington, DC, pp. 83–105.

Kohlstedt, D.L., Evans, B., Mackwell, S.J., 1995. Strength of the lithosphere – constraints imposed by laboratory experiments. J. Geophys. Res., Solid Earth 100, 17587–17602.

Lankford, J., 1996. High strain rate compression and plastic flow of ceramics. J. Mater. Sci. Lett. 15, 745–750.

Mecklenburgh, J., Heidelbach, F., Mariani, E., Mackwell, S., Seifert, F., 2010. Rheology and microstructure of $(Ca_{0.9},Sr_{0.1})TiO_3$ perovskite deformed in compression and torsion. J. Geophys. Res., Solid Earth 115 (B5). http://dx.doi.org/10.1029/2009JB006520.

Olgaard, D.L., Evans, B., 1986. Effect of second-phase particles on grain growth in calcite. Contrib. Mineral. Petrol. 69, C272–C277.

Passchier, C.W., Trouw, R.A.J., 2005. Micro-Tectonics. Springer, pp. 1–365.

Poirier, J.P., 1985. Creep of Crystals. Cambridge Earth Sciences Series, pp. 1–258.

Reches, Z., Lockner, D.A., 2010. Fault weakening and earthquake instability by powder lubrication. Nature 467, 452–502.

Ree, J.H., Ando, J.I., Han, R., Shimamoto, T., 2014. Coseismic microstructures of experimental fault zones in Carrara marble. J. Struct. Geol. 66, 75–83.

Rice, J.R., 2006. Heating and weakening of faults during earthquake slip. J. Geophys. Res., Solid Earth 111 (B5). http://dx.doi.org/10.1029/2005JB004006.

Rowe, C.D., Fagereng, A., Miller, J.A., Mapani, B., 2012. Signature of coseismic decarbonation in dolomitic fault rocks of the Naukluft Thrust, Namibia. Earth Planet. Sci. Lett. 333, 200–210. http://dx.doi.org/10.1016/j.epsl.2012.04.030.

Rutter, E.H., 1995. Experimental study of the influence of stress, temperature, and strain on the dynamic recrystallization of Carrara marble. J. Geophys. Res., Solid Earth 100, 24651–24663.

Rutter, E.H., 1999. On the relationship between the formation of shear zones and the form of the flow law for rocks undergoing dynamic recrystallization. Tectonophysics 303, 147–158.

Rutter, E.H., Brodie, K.H., 1988. The role of tectonic grain-size reduction in the rheological stratification of the lithosphere. Geol. Rundsch. 77, 295–307.

Rutter, E.H., Casey, M., Burlini, L., 1994. Preferred crystallographic orientation development during the plastic and superplastic flow of calcite rocks. J. Struct. Geol. 16, 1431–1446.

Schmid, S.M., Boland, J.N., Paterson, M.S., 1977. Superplastic flow in finegrained limestone. Tectonophysics 43, 257–291.

Scholz, C.H., 1998. Earthquakes and friction laws. Nature 391, 37–42.

Schubnel, A., Brunet, F., Hilairet, N., Gasc, J., Wang, Y.B., Green, H.W., 2013. Deep-focus earthquake analogs recorded at high pressure and temperature in the laboratory. Science 341, 1377–1380.

Sibson, R.H., 1977. Fault rocks and fault mechanisms. J. Geol. Soc. Lond. 133, 191–213.

Siman-Tov, S., Aharonov, E., Sagy, A., Emmanuel, S., 2013. Nanograins form carbonate fault mirrors. Geology 41, 703–706.

Smith, S.A.F., Billi, A., Di Toro, G., Spiess, R., 2011. Principal slip zones in limestone: microstructural characterization and implications for the seismic cycle (Tre Monti Fault, Central Apennines, Italy). Pure Appl. Geophys. 168, 2365–2393. http://dx.doi.org/10.1007/s00024-011-0267-5.

Smith, S.A.F., Di Toro, G., Kim, S., Ree, J.H., Nielsen, S., Billi, A., Spiess, R., 2013. Coseismic recrystallization during shallow earthquake slip. Geology 41, 63–66.

Smith, S.A.F., Nielsen, S., Di Toro, G., 2015. Strain localization and the onset of dynamic weakening in calcite fault gouge. Earth Planet. Sci. Lett. 413, 25–36.

Tisato, N., Di Toro, G., De Rossi, N., Quaresimin, M., Candela, T., 2012. Experimental investigation of flash weakening in limestone. J. Struct. Geol. 38, 183–199.

Valoroso, L., Chiaraluce, L., Collettini, C., 2014. Earthquakes and fault zone structure. Geology 42, 343–346.

Verberne, B.A., De Bresser, J.H.P., Niemeijer, A.R., Spiers, C.J., De Winter, D.A.M., Plumper, O., 2013. Nanocrystalline slip zones in calcite fault gouge show intense crystallographic preferred orientation: crystal plasticity at sub-seismic slip rates at 18–150 °C. Geology 41, 863–866.

Verberne, B.A., Plümper, O., Matthijs de Winter, D.A., Spiers, C.J., 2014. Superplastic nanofibrous slip zones control seismogenic fault friction. Science 346 (6215).

Walker, A.N., Rutter, E.H., Brodie, K.H., 1990. Experimental-study of grain-size sensitive flow of synthetic, hot-pressed calcite rocks. In: Deformation Mechanisms, Rheology and Tectonics, vol. 54, pp. 259–284.